Editors' Suggestion

Barrier bucket gymnastics and transversely split proton beams: Performance at the CERN Proton and Super Proton Synchrotrons

M. Vadai,[1,2] A. Alomainy,[2] H. Damerau,[1] M. Giovannozzi,[1] and A. Huschauer[1]

[1]*Beams Department, CERN, Esplanade des Particules 1, 1211 Geneva 23, Switzerland*
[2]*Queen Mary University of London, London E1 4NS, United Kingdom*

(Received 19 August 2021; revised 28 April 2022; accepted 9 May 2022; published 20 May 2022)

During the 2018 proton run, a new radio-frequency beam manipulation has been studied and successfully implemented at the CERN Proton Synchrotron (PS) for the first time. This technique is used to deplete a well-defined fraction of a continuous longitudinal beam distribution by creating a so-called barrier bucket. We propose a new application of the barrier bucket gymnastics in the multiturn extraction scheme used at CERN. These two exotic techniques are combined into a highly sophisticated procedure that dramatically reduces the beam losses at PS extraction, thus paving the way to high-intensity proton beams for future fixed-target experiments at the CERN Super Proton Synchrotron (SPS). In this paper, the expected performance of the PS and SPS is analyzed in detail to define a road map for making this novel extraction scheme operational.

DOI: 10.1103/PhysRevAccelBeams.25.050101

I. INTRODUCTION

Following the first proposal of transverse beam splitting to perform a fast extraction over subsequent turns [1], the multiturn extraction (MTE) scheme replaced the old continuous transfer (CT) extraction method [2–4] in the CERN Proton Synchrotron (PS). The operational implementation of MTE allowed one to significantly reduce extraction losses in the PS ring, and relentless efforts have been devoted to the optimization of MTE (see, e.g., Refs. [5–7]).

The difference in the circumference of the PS and the Super Proton Synchrotron (SPS), the latter 11 times longer than the first, imposes the extraction of the beam from the PS over multiple turns to maximize the duty factor for fixed-target experiments. It turns out that the optimum choice consists of extracting the PS beam over five turns. The CT [2] was designed to achieve this goal by shaving the beam onto the foil of an electrostatic septum with a clever system of magnets generating slow (over thousands of turns) and fast (over five turns) perturbations of the closed orbit, with the horizontal tune set to $Q_H = 6.25$. However, this approach had the drawback of generating losses and activating ring equipment due to the beam-foil interaction [3], not to mention the unavoidable difference in horizontal emittance [8]. MTE has been designed to split the beam into five beamlets in the horizontal plane by crossing the fourth-order resonance adiabatically [1,9]. In this way, the losses due to the beam-foil interaction are completely removed, and only those due to the longitudinal beam structure and the rise time of the extraction kickers remain.

Eventually, the overall performance of beams for the fixed-target physics program at the SPS, which are produced using the MTE scheme in the PS, should reach and possibly surpass that of CT. While this is already a reality in the PS, some work remains to be done in the SPS, where losses due to the high value of the vertical beam emittance are still observed [10,11].

The intense studies on the theory behind transverse beam splitting [12] had ensured that the PS performance is close to an optimum. Moreover, the recent activities devoted to the assessment of the PS and SPS performance in the presence of high-intensity beams [10,11] confirmed that no showstopper is in sight when pushing the intensity available for fixed-target physics at the SPS further. It will be made possible following the improvements along the CERN accelerator chain pursued in the framework of the LHC injectors upgrade (LIU) project [13]. All these activities will allow the implementation of new physics experiments in the SPS experimental area, such as the search for hidden particles [14,15]. Note that previous studies on the impact of indirect space-charge effects on MTE [16,17] have been particularly relevant in the context of high-intensity beams.

Given the successful campaigns to optimize MTE performance by reducing the amount of extraction beam losses to a level of 1%–2% in the PS, no further significant

improvement is expected by changing the available standard settings. Merely a better stability of the beam parameters delivered to the SPS might be achieved.

The remaining extraction beam losses are a consequence of the SPS requirements for the beam transfer from the PS, as a debunching gymnastic is performed after transverse beam splitting and prior to extraction. While this is mandatory from the standpoint of the SPS, it is certainly a drawback for the PS, given that the non-negligible rise time of the extraction kickers induces beam losses during beam extraction. A much more promising approach appears to be the implementation of a barrier bucket [18–23] that has the potential to practically reduce extraction losses in PS to zero. The advantage of this approach is that no new hardware is required, as a wideband rf cavity is already present in the PS ring. It is loaded with Finemet® material, which makes it usable in the frequency range from 400 kHz to well above 10 MHz. This device was installed in 2014 [24,25] as a part of longitudinal feedback.

The research in this direction has been actively pursued at the PS with extremely encouraging results [26–28]. It has been possible to successfully implement barrier bucket gymnastics in the PS and even merge it with the transverse beam splitting with a substantial reduction of beam losses at PS extraction. In this paper, the performance achieved will be reviewed in detail, not only in terms of measured beam losses, but also in terms of the longitudinal beam distribution obtained and its impact on PS and SPS performance.

The combination of transverse adiabatic trapping and longitudinal barrier buckets opens up new possibilities in the domain of multiturn extractions. Thanks to adiabatic trapping, it is possible to manipulate the horizontal emittance, so as to better adapt it to the acceptance of the receiving accelerator. Furthermore, beam splitting generates a beam structure that extends beyond the length of the accelerator circumference. In this way, extraction losses due to the transverse beam structure are reduced. The combination of transverse beam splitting with a barrier bucket makes it possible to perform a quasi-loss-free multiturn extraction, an essential feature for high-intensity proton beams.

Section II introduces a simple alternative to calculating the adiabaticity with moving barriers, which is consistent with previous studies [20,22] and was also simulated as well as confirmed experimentally.

The performance of the PS manipulation, which combines the transverse splitting with the barrier bucket [27], a unique technique, is analyzed in detail in Sec. III. In Sec. IV, the overall performance of the PS and SPS rings is presented and discussed.

II. BARRIER BUCKET MANIPULATION

Generating a gap in the, otherwise ideally constant, longitudinal particle density is performed with a pulsed rf system. This serves two purposes: It leaves most of the beam in a debunched state outside of the region of the pulse, while it creates a quasi-particle-free gap in the ring circumference. Both purposes are achieved by two main features of the rf waveform: the reflection region ϕ_r, where the normalized RF amplitude g is nonzero, and the drift space ϕ_d, where the amplitude is ideally zero (see Fig. 1). The longitudinal motion can be expressed in the coordinates of azimuthal position ϕ of the particle and its phase velocity $\dot{\phi}$ with respect to a particle at the reference energy, by means of a reduced Hamiltonian for an arbitrary rf amplitude [29]:

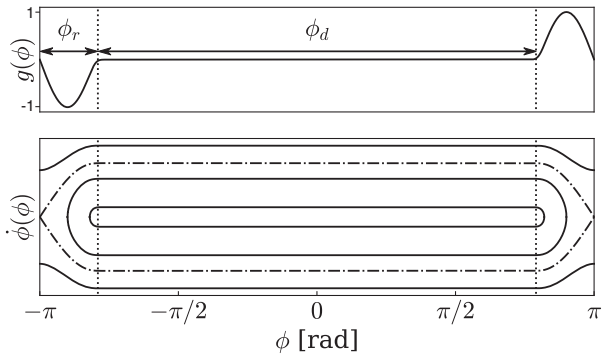

FIG. 1. The rf voltage normalized by the peak amplitude (top) of the pulsed rf system generating a barrier bucket with the reflection region ϕ_r and drift space ϕ_d. The bottom plot is the illustration of the corresponding trajectories in the longitudinal phase space, including the separatrix (dashed line).

$$H(\phi,\dot{\phi}) = \frac{1}{2}\dot{\phi}^2 + \omega_s^2 W(\phi) \tag{1}$$

with

$$W(\phi) = \frac{1}{\cos\phi_0}\left[\int g(\phi)d\phi - g(\phi_0)\phi\right]. \tag{2}$$

The potential $W(\phi)$ is generated by the normalized voltage $g(\phi)$ of the pulsed rf system. The stable phase ϕ_0 is arbitrarily chosen to be in the middle of the barrier bucket, and ω_s is the linear angular synchrotron frequency of the particle around the synchronous phase of a conventional bucket, which is equivalent to the reflection region of the barrier bucket. These variables help to derive a simple adiabaticity criterion for azimuthal barrier motion using a single-particle approximation.

A. Estimate of the phase-space area growth due to barrier bucket compression and expansion

Initially, two rebucketing schemes from a conventional rf system to the barrier rf system at extraction were considered, one by azimuthally moving barriers and the second by lowering the amplitude of the main rf system and increasing

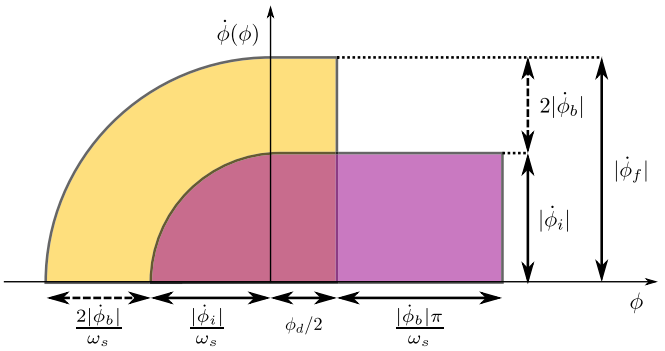

FIG. 2. Diagram of the quarter areas of the phase space before (purple) and after (yellow) a particle reflection off a moving barrier comparing fully filamented cases. The buckets are shifted and centered around the edge of the reflection region for before and after a reflection to allow an easy comparison of the area changes in the reflection region and the drift space. The two trajectories phase spaces are shifted such that the main parameters used in the calculation are visible.

the one of the barrier rf. Although there are derivations for barrier bucket compressions and decompressions [20,22], they are particularly well suited for higher barrier speeds. Here, a simple criterion based on a geometrical consideration for much lower barrier speeds than the phase velocity of an outer trajectory of a barrier bucket is developed.

To estimate the growth of the emittance during the compression and expansion of the barrier bucket, we studied the trajectory of a particle encircling the entire bunch. The surface within this trajectory represents the initial value of its invariant. Two of these surface values are evaluated, one before the interaction with the barrier and one after the interaction with the barrier. This interaction is assumed to happen during half of the linear synchrotron period in a traditional bucket, corresponding to the reflection region of the barrier bucket. The barrier moves during this time, and the drift space of the corresponding barrier bucket changes as illustrated in Fig. 2, while the bucket height stays constant. However, the phase velocity $\dot{\phi}$ of the particle changes before and after reflection, even with constant bucket height according to Eqs. (1) and (2). This simple analysis estimates the area encircled by a particle under these conditions before and after a single reflection, during the time the reflection takes place. If this area change is too large, that may indicate a nonadiabatic manipulation, in general. In particular, it does so if the bucket is filled with particles as in the tests below. This estimate does not assume multiple reflections and is restricted to single-particle dynamics, without intensity effects. In both cases, full filamentation is assumed. The following derivation has two parts corresponding to the two regions of the stationary barrier bucket. The first part describes the changes in the drift space by looking at the nature of the reflection of particles off a moving potential barrier. The second part describes the changes in the reflection region. Together, they provide a basis for estimates of the emittance growth and barrier speed limits.

The drift speed of the particle outside of the reflection region in phase space is the phase velocity $\dot{\phi}$. The phase velocity of the barrier is denoted as $\dot{\phi}_\mathrm{b}$, as the barrier moves along the ϕ axis. The barrier speed is assumed to be constant, as was the case during the beam tests reported in the following sections of this article.

Looking at the dynamics of one reflection, it is evident that the phase velocities before and after a reflection are equal in modulus and of opposite sign for the case of a stationary barrier. This motion is mathematically identical to an elastic collision of a point particle with a stationary wall of infinite mass in a nonrelativistic approximation. However, when the wall moves with a constant nonzero velocity v_wall in the observer's reference frame, the velocities before (v_i) and after (v_f), according to the classical Galilean transformation, whose use is justified by the low speeds involved, are the following:

$$v_\mathrm{i} + v_\mathrm{f} = 2v_\mathrm{wall}. \tag{3}$$

These speeds do not depend on the details of the reflection, we assume only that the interaction happens, and the energy and momentum are conserved. This is also the assumption that is made for the phase velocity of a particle in phase space, where the wall becomes the moving barrier:

$$\dot{\phi}_\mathrm{i} + \dot{\phi}_\mathrm{f} = 2\dot{\phi}_\mathrm{b}, \tag{4}$$

and this relationship holds for an arbitrary voltage shape, as long as its amplitude guarantees that the particle is reflected (of course, the probability of tunneling through the barrier is negligible).

During reflection, the drift space gets shorter in case of compression or longer in case of expansion. The time it takes for a particle to be reflected can be approximated by half of a synchrotron period $T_\mathrm{s}/2 = \pi/\omega_\mathrm{s}$ of a conventional rf bucket corresponding to the reflection region of the barrier bucket. At the same time, the barrier phase moves half of the synchrotron period, i.e., by $\dot{\phi}_\mathrm{b} T_\mathrm{s}/2 = \dot{\phi}_\mathrm{b}\pi/\omega_\mathrm{s}$.

To estimate the change of emittance in the reflection region, a linear voltage is assumed for a stationary bucket. This is justified, since the essential particle dynamics in a barrier bucket does not depend on the shape of the voltage used but only on the integral of the voltage [20]. For the simple case of linear rf voltages, the trajectories in the longitudinal phase space become ellipses. The following geometrical argument can, therefore, be used to estimate the emittance growth before and after a single reflection looking at the initial and final filamented trajectories.

At the beginning of the compression, an initial phase relative to the edge of the reflection region, ϕ_0, is assumed;

see also Fig. 1. Note that $\phi_0 = \phi_d/2$, where ϕ_d is the initial drift space length. Then using Eq. (4) and the notation of Fig. 2, the ratio of the two colored areas A_i and A_f, representing the change in longitudinal emittance before and after reflection, respectively, is evaluated to

$$\frac{A_\mathrm{f}}{A_\mathrm{i}} = \frac{|\dot{\phi}_\mathrm{f}|(|\dot{\phi}_\mathrm{f}|\pi + 2\phi_\mathrm{d}\omega_\mathrm{s})}{(|\dot{\phi}_\mathrm{f}| - 2|\dot{\phi}_\mathrm{b}|)[(|\dot{\phi}_\mathrm{f}| - 2|\dot{\phi}_\mathrm{b}|)\pi + 4|\dot{\phi}_\mathrm{b}|\pi + 2\phi_\mathrm{d}\omega_\mathrm{s}]}. \tag{5}$$

It is worth noting that the phase change due to the change of a trajectory $2|\dot{\phi}_\mathrm{b}|/\omega_\mathrm{s}$ in the reflection region is not the same as the phase change in the drift region, due to the displacement of the barrier $|\dot{\phi}_\mathrm{b}|\pi/\omega_\mathrm{s}$. The singularity for $\dot{\phi}_\mathrm{f} = 2\dot{\phi}_\mathrm{b}$ is the case when a beam in a long barrier bucket turns into a beam in a conventional rf bucket in $T_\mathrm{s}/2$ time or vice versa. This provides a hard limit on the barrier speed for an adiabatic manipulation; see Fig. 3 (right). If the area occupied by the particles in the phase space changes too fast, the manipulation will become nonadiabatic; therefore, the barrier speed should correspond to a very small area change during one reflection—see Fig. 3 (left). Using the notations in Fig. 1, $\phi_\mathrm{r} = \dot{\phi}_\mathrm{f}/\omega_\mathrm{s}$. The estimated emittance growth corresponding to different $\phi_\mathrm{d}/\phi_\mathrm{r}$ barrier bucket aspect ratios can also be seen in Fig. 3 (left).

It is clear that the barrier speed should be much lower than the drift speed of a particle with maximum energy offset, which means $\dot{\phi}_\mathrm{b}/\dot{\phi}_\mathrm{f} \ll 1$ [20]. This is the limiting case of a particle that is not interacting with the potential barrier at all, as it never enters the reflection region. Following the geometric considerations above, also illustrated in Fig. 3 (right), the barrier speed must ideally be chosen below half of that value [22] to avoid significant growth of the emittance during manipulation. Barrier speeds relative to the maximum phase velocity, $\dot{\phi}_\mathrm{b}/\dot{\phi}_\mathrm{f}$, on the order of a few percent correspond to a few percent increase of the occupied phase-space area during reflection at the barrier (Fig. 3, left). This results in a quasiadiabatic manipulation.

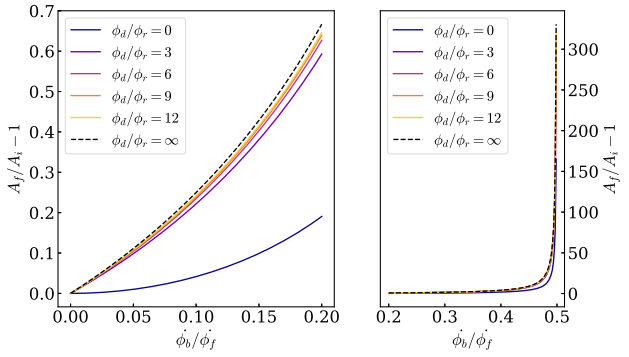

FIG. 3. Left: phase-space area ratio estimate for low relative barrier speeds. Note that at zero barrier speeds the growth per reflection is exactly zero. Right: limiting case of the relative barrier speed at half of the phase velocity of an outer particle in the bunch; on this scale, all curves converge to the singularity regardless of the $\phi_\mathrm{d}/\phi_\mathrm{r}$ bucket aspect ratios.

B. Low-energy and low-intensity PS beam studies

Beam tests with azimuthally moving barriers were conducted in the PS during the commissioning of the barrier rf system in the PS at injection energy $E = 1.4$ GeV (kinetic) and allowed bench marking of the adiabaticity limits estimated above. The comparison of measurements and analytical estimates is reported in Ref. [28], while numerical simulations and their comparison with analytical estimates are presented here.

Longitudinal particle tracking simulations using BLonD [30] were developed in addition to performing particle tracking under the same conditions as for measurements. The pulsed rf voltage was modeled in simulations as a Fourier sum of 25 harmonic components with a peak value of 3 kV, matching the waveform generated by the hardware [26]. To avoid Gibbs oscillations leading to microbunching in the drift region, Lanczos σ factors (see pp. 75–80 in Ref. [31]) were used to improve the convergence of the Fourier series, making better use of the available bandwidth. This synthesis method was furthermore beneficial, because it presents no added computational overhead in the simulation at run-time. Intensity effects can be ignored in these simulations, since initial tests were performed with a low-intensity beam of 10^{10} particles per pulse, where the induced voltage is negligible compared to the amplitude of the barrier waveform.

The evolution of the longitudinal profile with the relative phase velocity $\dot{\phi}_\mathrm{b}/\dot{\phi}_\mathrm{f}$ of 0.01 and 0.25, corresponding to the two ends of the speed range probed, was simulated and is displayed together with the measured data in Figs. 4 and 5, respectively. Simulations agree with the measured data to a high degree, and both confirm the analytically predicted speed limits. These considerations are particularly relevant

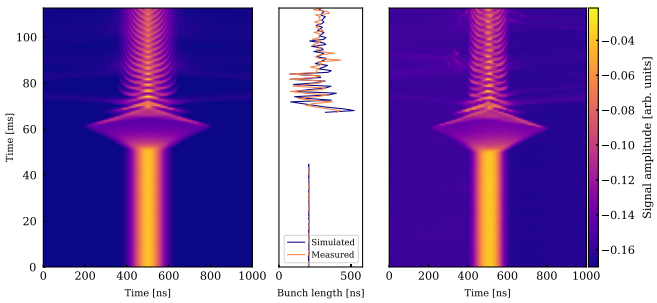

FIG. 4. Evolution of the bunch profile during fast expansion and compression at a normalized speed of $\dot{\phi}_\mathrm{b}/\dot{\phi}_\mathrm{f} \approx 0.25$. The oscillations after 60 ms are a clear indication for a nonadiabatic manipulation. Simulated (left) and measured (right) profiles are shown with their corresponding bunch lengths.

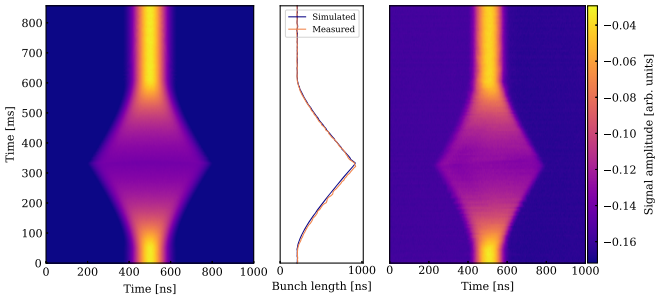

FIG. 5. Evolution of the bunch profile during slow expansion and compression at a normalized speed of $\dot{\phi}_b/\dot{\phi}_f \approx 0.01$. The smooth transitions indicate an adiabatic manipulation. Simulated (left) and measured (right) profiles are shown with their corresponding bunch lengths.

for the handover from the conventional to the barrier bucket as introduced in Sec. III B.

III. COMBINING TRANSVERSE BEAM SPLITTING AND BARRIER BUCKET

A. The acceleration cycle for the fixed-target beam in the PS

Injection into the PS occurs from the upstream PS booster (PSB), which consists of four rings stacked vertically with ring 1 being that at the bottom and ring 3 being at the same height as the PS. The beams from rings 3, 4, 2, and 1 are subsequently injected, with the principal harmonic number being $h = 2$ in the PSB. In 2018, the injection into the PS took place at 1.4 GeV kinetic energy and, following the upgrades implemented by the LIU project, will be increased to 2.0 GeV in 2021.

Since the PS circumference is 4 times as long as that of the PSB, the bunch-to-bucket transfer in the PS requires an rf capture at $h = 8$. To suppress longitudinal instabilities during the PS cycle, a controlled longitudinal emittance blowup with a phase-modulated 200 MHz system is performed. After accelerating to an intermediate magnetic plateau with a momentum of 3.5 GeV/c, an additional longitudinal emittance blowup is applied to mitigate instabilities when crossing the transition. At the same time, a splitting from 8 to 16 bunches is accomplished by changing the main harmonic to $h = 16$. The beam is then accelerated through the transition energy to the magnetic flattop at 14 GeV/c. A debunching process is realized by decreasing the amplitude of the main rf system at 7.6 MHz ($h = 16$) down to zero. At the end of the cycle, just before extraction, the 200 MHz system is pulsed at full voltage for about 1 ms to modulate the longitudinal beam structure and ease capture with the main SPS 200 MHz rf system.

B. Rebucketing into a barrier bucket

The operational configuration was modified for the joint, i.e., in both PS and SPS, beam tests, whose aim was to include both manipulations, namely, the barrier bucket and MTE. Because of the long synchrotron periods in barrier buckets, also confirmed by the low-energy compression and decompression tests, the amplitude modulation scheme for the handover from the conventional rf system to the barrier bucket rf was chosen. Therefore, the transfer to the barrier bucket rf system [27,28] instead of complete debunching was initially added without transverse beam splitting. This temporary configuration allowed advancing the rebucketing into the barrier bucket to gain time for measurements conducted using the wall current monitor (WCM) installed in the PS as shown in Fig. 6.

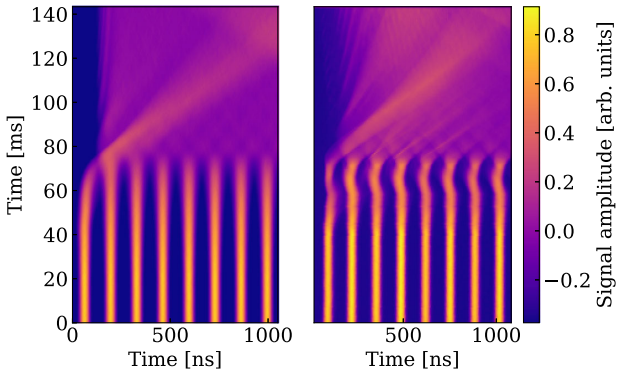

FIG. 6. Beam reflecting off a potential barrier, shown over half a PS turn. The amplitude of the $h = 16$ system was lowered and then subsequently turned off at 70 ms, and the amplitude of the barrier bucket rf system was increased to reach the maximum at the same time. The transverse beam splitting was disabled during these measurements. Simulated (left) and measured (right) profiles are shown.

Note that the barrier bucket rf system was operated at the maximum available rf power, without an amplitude-control loop. Therefore, the peak voltage is slightly dependent on the gap size, since the system delivers different peak amplitudes for different configurations of harmonics. Beam loading can, moreover, reduce the available voltage by about a fifth at the highest intensities. During subsequent tests, the timings were adjusted to properly include the duration of the transverse beam splitting, without the transverse splitting itself actually being enabled. It is worth noting that the longitudinal motion is not directly affected by the transverse one. However, this is not the case for the transverse motion. Therefore, by turning the transverse beam splitting on, no significant change in the longitudinal beam dynamics was expected, as will be seen in the next section.

C. Low- and high-frequency modulation of the longitudinal profiles and gap shoulders

It is worth recalling that MTE generates a split beam made of five beamlets: four corresponding to the stable islands and the fifth corresponding to the beam left around the origin of the phase space. Since the WCM measures

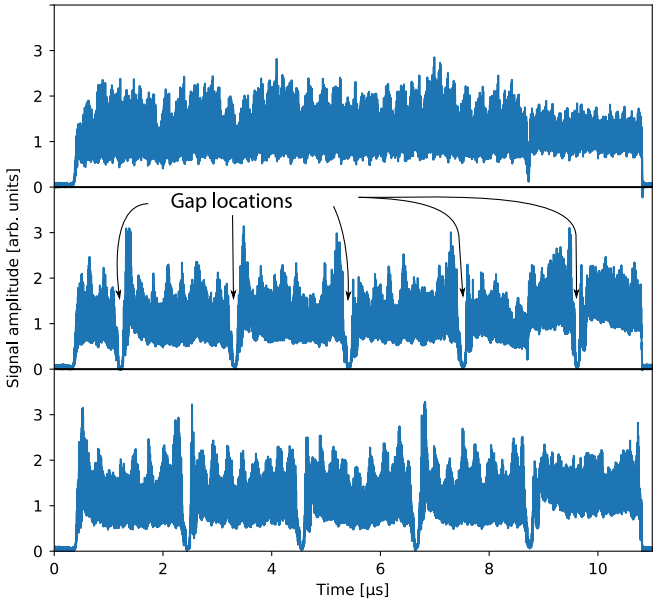

FIG. 7. Examples of the longitudinal beam structure measured in the transfer line without a barrier bucket (top), with an asynchronous barrier bucket (middle), and with a synchronous barrier bucket (bottom) compared to the rise of the PS extraction kickers. The 200 MHz modulation is clearly visible.

only the superposition of the five transverse beamlets, the effect of combined beam manipulation can be studied in detail only in the transfer line connecting the PS with the SPS. The five beamlets are extracted from the PS in consecutive turns, separated in time. An additional point to be considered is that, during the joint beam tests in the PS and SPS, the synchronization of the position of the barrier bucket with the rise of the PS extraction kickers was not yet possible for technical reasons. This means that the relative position between the rise of the PS extraction and SPS injection kickers, which are fixed with respect to each other, and the barrier bucket was fluctuating randomly from cycle to cycle. Three examples of the measured longitudinal beam profile in the TT2 transfer line between PS and SPS are shown in Fig. 7. A typical longitudinal beam profile without a barrier bucket is shown in the top plot. Two features are worth mentioning. First, increased intensity fluctuations occur during the first four extracted turns. Their origin is being studied, and they are probably caused by a combined effect of the tune resonance combined with the excitation by the transverse feedback. Second, a very short longitudinal gap is due to the rise of the two extraction kickers KFA4 and KFA71 used to extract the central beamlet on the fifth turn. A profile corresponding to the barrier bucket position being asynchronous with the rise of the extraction kickers is visible in the middle plot. The gap region of the barrier bucket can be seen in the unfolded beam structure. In this case, five additional gaps are visible in the longitudinal beam profile, and their position is separated in time by a single PS turn at 14 GeV/c, i.e.,

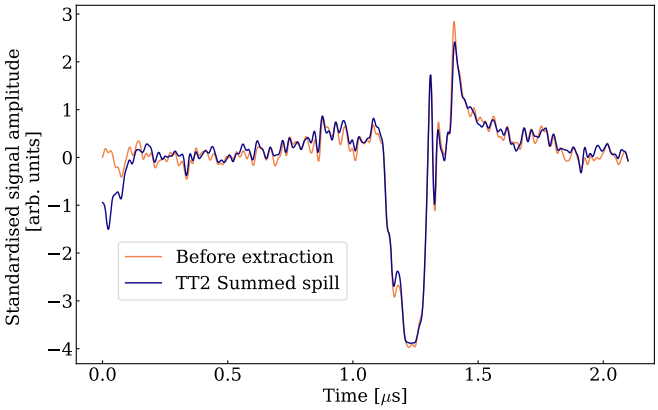

FIG. 8. The summed profiles from the fast beam current transformer in the TT2 transfer line compared with the WCM trace before extraction.

2.1 μs, as the transfer trigger moves from cycle to cycle in time with respect to the azimuthal position of the gap. The bottom plot in Fig. 7 shows a case where the barrier bucket is approximately synchronous with the kicker rise times, which occurred only accidentally during these measurements. This is, however, the desired operational condition, which is to be realized by developing a suitable synchronization scheme.

To study the origin of the spikes observed on the extracted beam profiles, the measurements in the ring recorded just before extraction were compared with the profiles in the transfer line with the barrier bucket rf system being either enabled or disabled. The five-turn-long profiles measured in the transfer line were summed turn by turn and aligned in phase with the profile measured in the PS ring, when the islands and the core are longitudinally still folded into a single structure.

Figure 8 illustrates a typical example of longitudinal beam profiles before extraction (pink line) compared to the sum of the five turns after extraction (blue line). The profiles are almost identical. The high-frequency modulation near the gap region, called a spike, is consistently present in both traces. There is, as expected, a slight difference during the first few tens of nanoseconds: The drop in the line density corresponds to the rise time of the extraction kickers, 350 ns for the islands and 56 ns for the core [32], and is systematically present in the typical case when the barriers were not synchronized with the extraction process.

To demonstrate that the similarity of the profiles is close to the example shown in the entire measured dataset and to avoid manually aligning the beam profiles in time, the cross-correlation is calculated for different time offsets. The maximum cross-correlation is assumed to indicate the best possible time alignment of the measurements. Note that, when the normalized signals are equal, the maximum value of their cross-correlation is equal to 1, while no correlation gives 0. For example, the maximum value of the cross-correlation sequence of almost identical traces marked in

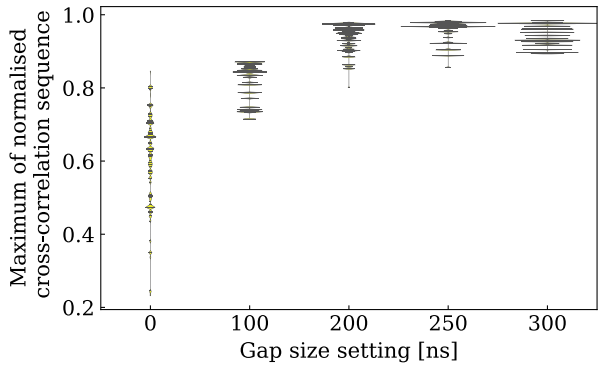

FIG. 9. The maximum of the cross-correlation sequence of the last acquisition before extraction from the PS and the summed five-turn profiles measured in the transfer line, standardized. Each thin, horizontal line represents a pair of observations. In this systematic analysis of the profiles similar to Fig. 8, when the main feature of the profiles is the gap itself, the similarity is larger. This means that the losses at extraction are a smaller fraction of the profiles compared to the beam displaced by the barrier during one turn. Therefore, the loss reduction when the barriers are synchronized with the kickers and the SPS injection is expected to be effective even at moderate gap size.

pink and blue in Fig. 8 is 0.97. These correlation values are compared for the whole dataset in Fig. 9.

The limited time available for rebucketing from the conventional $h = 16$ buckets to the barrier bucket, combined with the low synchrotron frequency, means that there is no time for the beam to filament in the barrier bucket [28]. Simulations indicate that the accumulation of line density near the barrier is mostly due to the particles being displaced from the gap region into the drift space, as the filamentation process is slow compared to the time of the manipulation. This results in the formation of shoulders on the bunch profile, i.e., regions with larger line density close to the barriers. The simulations are in good agreement with the measured data [27].

Interestingly, it was observed that the variation in line density at the edge of the drift space decreases with increasing intensity and improves the quality of the longitudinal spill. To show that this observation is not just due to a shot-to-shot variation, a method of evaluating the shoulders of the line density was developed. Gap positions were detected in the measured profiles by cross-correlating them with an ideal bunch profile calculated for each test case assuming a local elliptic energy distribution [33] that matches the acquisition parameters. This was necessary because of the perturbations or spikes of the profiles present in the gap region. It is necessary to identify the gap and drift regions in order to perform the normalization to compare the profiles with respect to the relative size of the shoulders. Line-density profiles were low-pass filtered to remove the 200 MHz component while preserving their overall shape. The profiles were then normalized such that the height of the line density between the middle of the drift space and the minimum of the line density is equal to one. As an example, Fig. 10 shows all traces acquired at the same moment across different cycles for the case of 180 ns gap setting, ordered by beam intensity. Based on simulations, the increased beam-induced broadband voltage causes an asymmetry in the shoulder regions, resulting in a narrower peak at the head of the bunch. This effect can be observed

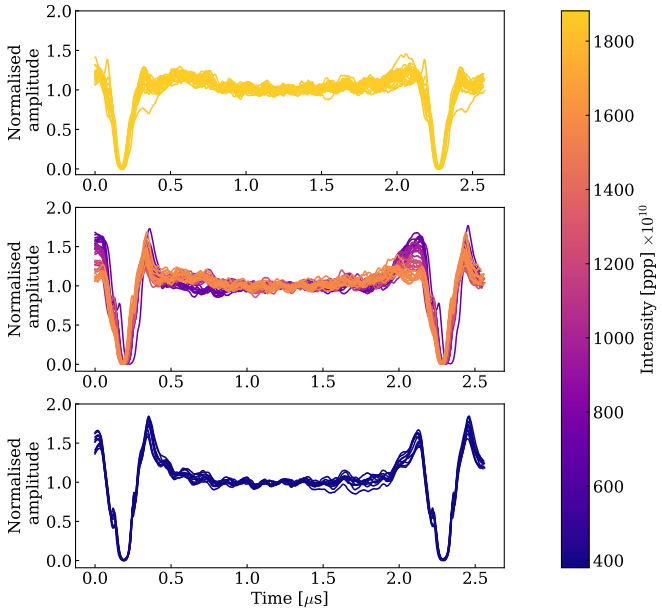

FIG. 10. Comparison of the low-pass filtered, normalized longitudinal line-density profiles at extraction at the same time in the rebucketing process for different acquisitions. The effect of the beam intensity on the line density and especially on the shoulders at the barrier edges can be seen for the same 180 ns gap size setting.

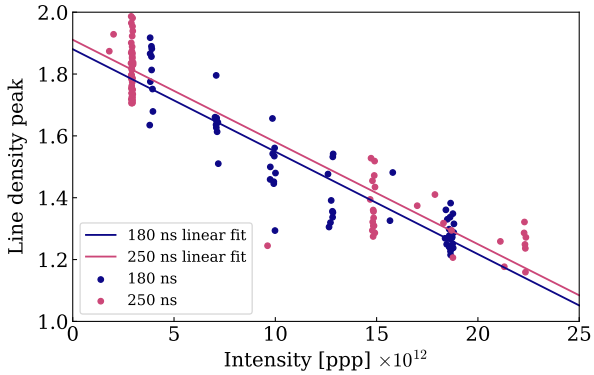

FIG. 11. Normalized line-density modulation along the bunch, showing a decreasing trend with increasing intensity. The colors refer to the different gap duration settings as indicated in the legend, which match the observed gap width well. Independent of the gap duration, the line-density modulation improves with increasing intensity. 63 and 76 acquisitions for 180 and 250 ns are shown, respectively. The least-squares linear fits are plotted to highlight the downward trend.

in Fig. 11 comparing the profiles from bottom to top. Line-density peaks near the barriers are smeared out at high intensity, resulting in a generally flatter longitudinal profile. This particular aspect of the dependence on intensity is subject to further studies with beam. Particle tracking simulations indicate that the phenomenon is not longitudinal space-charge related or related to the effect of cavity impedances. Further studies with beam are required, in particular, to gather more data with larger gap sizes in order to rule out not fully depleted reflection regions during this nonadiabatic process.

IV. BEAM TRANSFER TO THE SPS

A. General considerations

Toward the end of the 2018 proton run, a beam test was performed in which the barrier bucket scheme was implemented on the operational MTE cycle in the PS, and the beam was then sent to the SPS for a bit more than one hour to evaluate its performance. The evolution of PS extraction losses during this limited period is summarized in Fig. 12, together with the programmed width of the gap in the longitudinal beam distribution generated by the barrier bucket. As explained in Sec. III C, there was no synchronization mechanism between the kicker rise time and the barrier bucket position, leading to random shot-to-shot variations.

The beam losses are measured by two beam loss monitors (BLMs) installed in straight sections (SSs) 15 and 16 (see, e.g., Ref. [11] for more detail), i.e., the section immediately upstream and the one where the magnetic extraction septum is installed, respectively. In order to shadow the blade of the magnetic extraction septum in SS16, a passive device made of a copper blade is installed in SS15, which is enclosed by a specially designed concrete shielding. This creates a localized and well-shielded loss region, thus protecting the area around the magnetic extraction septum. The implementation of a barrier bucket scheme would render this installation obsolete, and the removal of this device would also significantly simplify the setup of other operational beams, which currently have to circumnavigate the blade for extraction.

During the initial phase of the experimental test, the losses in SS15 were higher than in SS16, indicating the intended protection of the extraction septum. Then, the copper blade was put in the parking position, i.e., removed from the ring aperture occupied by the beam, causing a drop of the beam losses in SS15 to nearly zero while considerably raising those in SS16. An important characteristic of the BLM system is that the integrated signal saturates, for technical reasons, at a value of 255 (corresponding to $2^8 - 1$), making it impossible to compare the absolute extraction losses in SS16. Note that the few points well below the saturation level are not outliers but rather correspond to the cycles for which the barrier bucket was more or less well synchronized with the raise of the PS extraction kickers.

B. PS extraction losses

The relative PS extraction efficiencies for the various configurations probed during the tests are shown in Fig. 13. These efficiencies were computed by comparing the measurement of the ring beam current transformer (10 ms before extraction) with that of a transformer in the transfer line. Violin plots are used whenever more than ten data points are available for a given configuration to provide information about the distribution of the data collected. From the complete dataset shown in Fig. 12, only the subset for which the passive blade in SS15 was moved to the parking position was considered for the analysis. The following configurations were extracted from this reduced dataset. (i) Cycles without any barrier bucket, which occurred inadvertently when switching from one value to another of the size of the gap. (ii) Cycles with the barrier bucket present at different programmed gap sizes, i.e., either 200 or 250 ns. (iii) In case there was a barrier

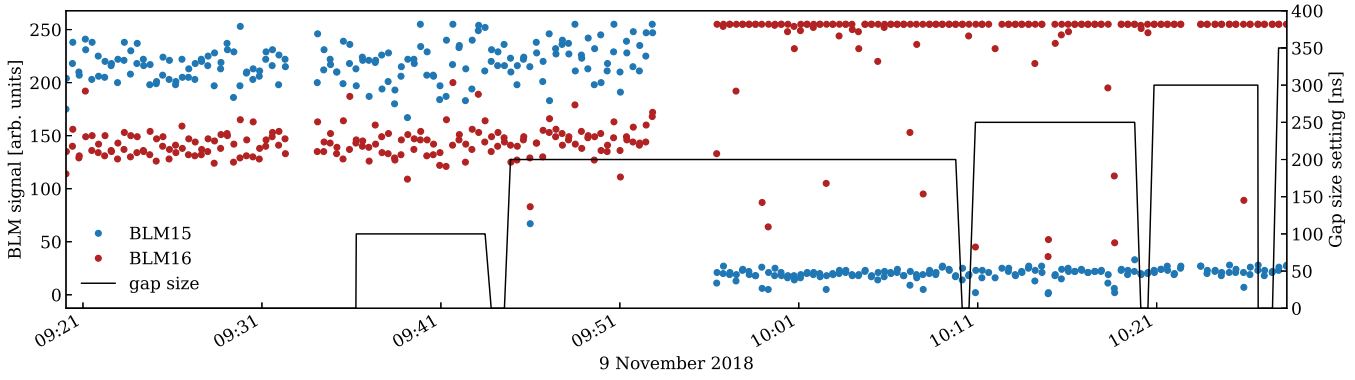

FIG. 12. Evolution of beam losses at PS extraction, measured by means of beam loss monitors installed in SS15 and 16, together with the programmed width of the gap generated in the longitudinal beam distribution by the barrier bucket during the experimental tests. The sudden drop of the BLM15 signal and simultaneous saturation of the BLM16 signal correspond to the copper blade set to parking position.

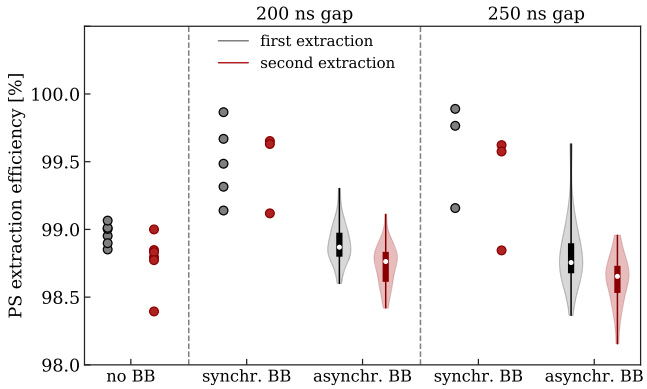

FIG. 13. PS relative extraction efficiency measured during the tests performed with the barrier bucket for several configurations. Datasets including more than ten samples are shown using violin plots.

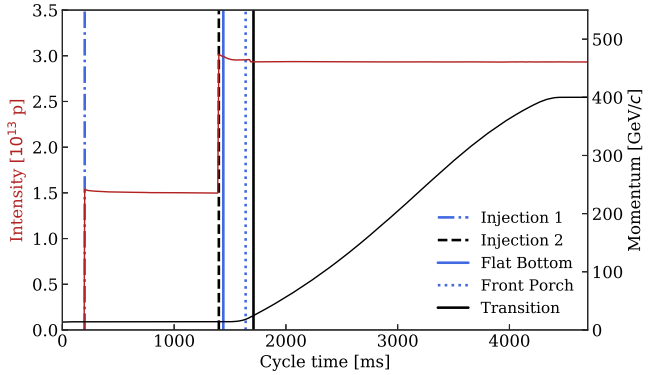

FIG. 14. Example of beam intensity in the SPS as a function of time together with the evolution of the beam momentum. The vertical lines indicate the different stages at which the relative transmission efficiencies are evaluated.

bucket, another distinction was made between synchronous and asynchronous cycles. As shown in Fig. 7 (middle), an asynchronous PS extraction is characterized by the longitudinal depletion region being replicated five times. In case of synchronization between the barrier bucket and extraction kickers, although this might occur only randomly, only four gaps are visible in the longitudinal distribution.

In addition to these three configurations, the operational SPS fixed-target beam production requires two subsequent extractions from the PS to fill in total 10/11 of the SPS-ring circumference. Therefore, the analysis also distinguishes between the first or the second injection into the SPS.

It is worth stressing that, depending on the actual gap size, the synchronization between the depletion region and the rise time of the PS extraction kickers has a margin of some tens of nanoseconds. Hence, even an imperfect synchronization can lead to reduced extraction losses in the PS ring, as demonstrated by the best achieved asynchronous extraction efficiency of the first extraction with a gap width of 250 ns.

The analysis reveals a systematically lower extraction efficiency for the second PS extraction, which is linked to the fact that the settings of the two PS cycles are fully identical but should be different. This is because, ideally, one would perform independent adjustments to account for dynamic effects, such as magnetic hysteresis, which is currently not being done. Furthermore, and as expected, no significant difference in efficiency is observed between extractions without the barrier bucket or with the asynchronous barrier bucket. On the other hand, the extraction efficiency clearly improves with the presence of a well-synchronized longitudinal gap. The difference between the two gap sizes appears to be minor. This implies that a final decision on the gap width might be based on other considerations, such as the beam performance in the SPS as a function of the gap width.

C. Current SPS performance

The SPS performance can be assessed by means of the definition of key times along the magnetic cycle, between which the relative transmission efficiencies are evaluated. The classification of the different stages and their times within the cycle are defined in the following way: (i) First and second injection (injections 1 and 2), referring to the injection efficiency of each individual PS extracted beam (the two injections are separated by 1.2 s); (ii) flat bottom, referring to the moment at the end of the flat bottom, 40 ms after the second injection (injection 2); (iii) front porch, referring to 200 ms after the flat bottom, when particles outside the rf buckets have been lost; (iv) transition, referring to 70 ms after the front porch. These times can be seen in Fig. 14, where the typical evolution of the beam intensity and momentum are shown as a function of time. Note that the transmission efficiencies (ii)–(iv) are defined in terms of the transmission from the previous stage to the stage named. As an example, transmission at transition is defined as the percentage of transmitted intensity from the front porch to a few milliseconds after the transition crossing.

Figure 15 shows the relative losses measured for the first and second injections in the SPS (top left) and on the flat bottom (top right) as a function of the width of the longitudinal gap. In both cases, no clear trend is visible for gap sizes below 250 ns, whereas a slight increase of losses starts from gaps of 300 ns and beyond.

The situation changes when losses through the energy ramp are considered, as can be seen in Fig. 15 (lower). The dependence of relative losses on the width of the gap is clearly visible in terms of both an increased spread of the loss distribution and an increased median value. Furthermore, the relative losses in the front porch have an increase for gap widths larger than or equal to 250 ns, while transition crossing losses already increase for a gap width of 200 ns. Contrary to Fig. 13, the plots shown in

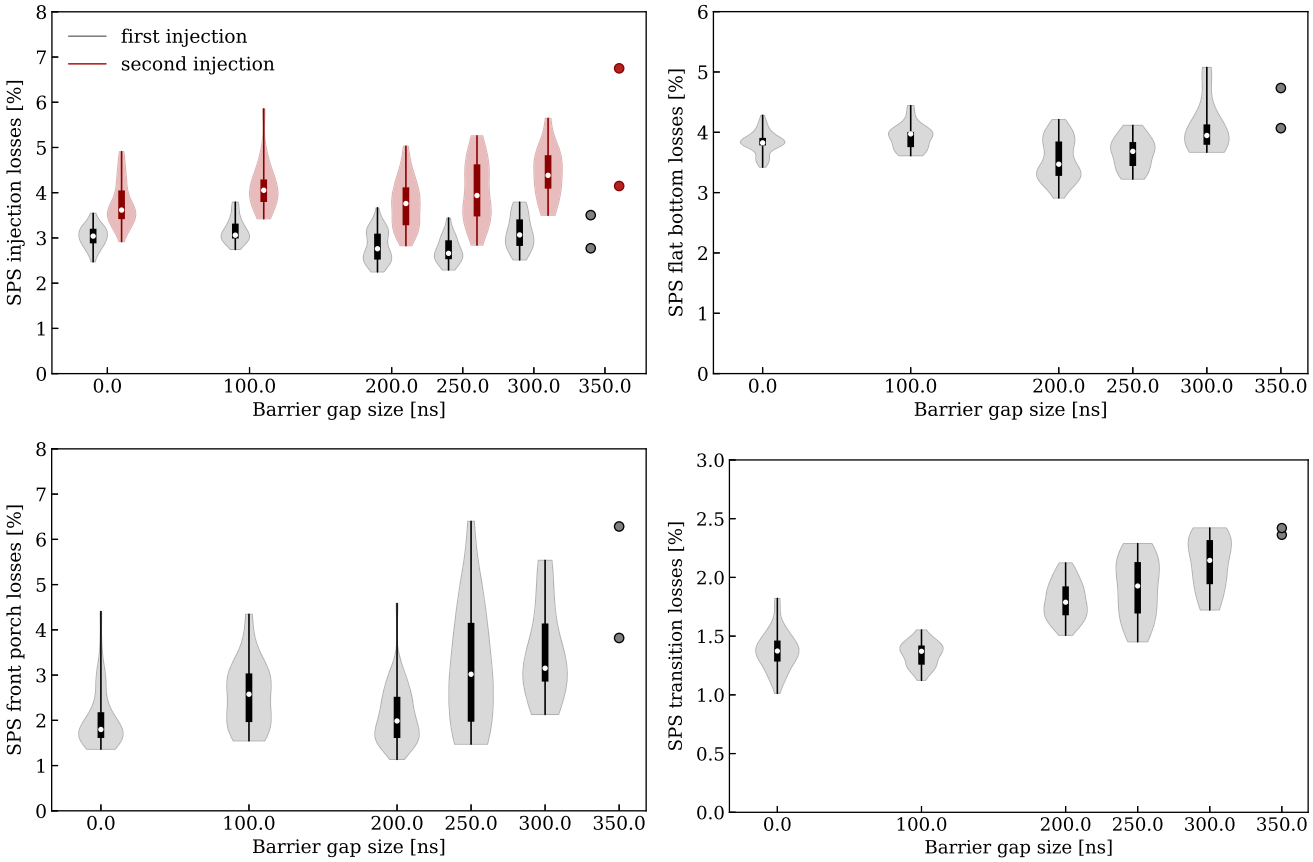

FIG. 15. Relative losses for the first and second injections (upper left) and during the flat bottom of the cycle (upper right) as a function of the width of the longitudinal gap in the beam distribution generated in the PS. No trend is visible up to a gap size of 250 ns, while a slight increase is observed for larger gaps. The lower plots show relative losses for front porch (left) and transition (right) as a function of the width of the longitudinal gap. A clear dependence on the gap width is observed.

Fig. 15 do not distinguish between synchronous and asynchronous gaps in the longitudinal beam distribution. From the analysis performed distinguishing the two cases, no clear differences emerged, which could also be due to the scarce statistics available for the synchronous case.

D. Longitudinal limitations and future improvements

Previous studies of intensity limitations for the fixed-target beam in the SPS [34,35] show an important uncontrolled longitudinal emittance blowup due to a single bunch instability after transition crossing, by approximately a factor of 2.5. At the typical 2018 operational intensity of about 3×10^{13} protons accelerated per cycle, this can be tolerated and actually leads to an increase of the momentum spread at flattop, which is beneficial for the slow extraction. This strong instability, however, leaves little margin for a future intensity increase, as the uncontrolled blowup must first be mitigated.

Additional beam gaps in the SPS introduce two main challenges with respect to the conventional fixed-target beam, which may affect the performance. First, the density of the longitudinal line must be increased to compensate for the empty gaps and restore the same accelerated total intensity. Second, the additional empty regions due to the barrier bucket manipulation introduce transient beam loading. These transients spaced by one PS revolution period must be handled by the rf system.

With the major upgrade of the SPS rf systems in the framework of the LIU project [13,36], the traveling wave structures of the main acceleration system have been reconfigured from four longer to six shorter structures, adding two new rf amplifiers with peak power of 1.6 MW at 200 MHz each. Improved feedback systems have been installed to reduce the beam-induced voltage to compensate for transient beam loading.

Furthermore, the upgrade of the longitudinal beam control and low-level rf systems will allow the operation of the higher-harmonic 800 MHz rf system in combination with the main accelerating system at 200 MHz for the fixed-target beam, which was excluded for technical reasons until 2018, before the upgrades by LIU. Based on experience with LHC-type beams [37,38], the double-harmonic rf will significantly increase longitudinal stability and reduce the loss of the fixed-target beam in the SPS.

V. CONCLUSIONS

The results of successful tests combining the transversely split beam with a new barrier bucket gymnastics in the PS have been reported in this paper, including the global performance assessment in PS and SPS. The analysis of beam dynamics in the barrier bucket, the impact of the longitudinal beam profile, and the gap generated on the beam losses throughout the SPS cycle have been studied in detail. Even assuming no improvement with respect to the conditions of the past beam tests, it is possible to reduce the losses at extraction in the PS, with only a mild increase of the losses in the SPS, in particular, at the transition crossing.

During the CERN long shutdown 2 (LS2), the LHC injector upgrade project [13] implements major upgrades in all LHC injectors. In particular, the activities in the SPS aim to improve the performance of the rf system [39], with the reduction of beam loading in the main accelerating cavities. The previously made assumptions, i.e., neglecting any upgrades taking place in the different accelerators, are, therefore, conservative. An important improvement in beam loss in both PS and SPS is expected. This would open the way to further increase the intensity for the fixed-target experiments at the SPS.

A vigorous experimental campaign will be carried out after the beam commissioning phase after LS2 to assess the impact of upgrades on beam quality with combined barrier bucket and transverse beam splitting. The implementation of a synchronization mechanism between PS and SPS will ensure the systematic alignment of the longitudinal gap with the rise of the PS extraction kickers. Finally, optimizing both transfers between PS and SPS separately will push the overall performance of this sophisticated beam process to its maximum.

ACKNOWLEDGMENTS

We thank the PS and SPS teams of the operations group for the support during the experimental measurements, as well as E. Shaposhnikova for her valuable input to the manuscript. The authors thank M. A. Fraser for the inspiring discussions on extraction and the use of barrier buckets. M. G. thanks F. Cerutti for several fruitful discussions on energy deposition and irradiation to accelerator components, and M. V. thanks A. Lasheen for the discussions related to longitudinal space-charge effects.

[1] R. Cappi and M. Giovannozzi, Novel Method for Multiturn Extraction: Trapping Charged Particles in Islands of Phase Space, Phys. Rev. Lett. **88**, 104801 (2002).

[2] C. Bovet, D. Fiander, L. Henny, A. Krusche, and G. Plass, The fast shaving ejection for beam transfer from the CPS to the CERN 300 GeV machine, IEEE Trans. Nucl. Sci. **20**, 438 (1973).

[3] J. Barranco García and S. Gilardoni, Simulation and optimization of beam losses during continuous transfer extraction at the CERN Proton Synchrotron, Phys. Rev. Accel. Beams **14**, 030101 (2011).

[4] J. Borburgh, S. Damjanovic, S. Gilardoni, M. Giovannozzi, C. Hernalsteens, M. Hourican, A. Huschauer, K. Kahle, G. Le Godec, O. Michels, and G. Sterbini, First implementation of transversely split proton beams in the CERN Proton Synchrotron for the fixed-target physics programme, Europhys. Lett. **113**, 34001 (2016).

[5] A. Huschauer, M. Giovannozzi, O. Michels, A. Nicoletti, and G. Sterbini, Analysis of performance fluctuations for the CERN Proton Synchrotron multi-turn extraction, J. Phys. Conf. Ser. **874**, 012072 (2017).

[6] S. Abernethy, A. Akroh, H. Bartosik, A. Blas, T. Bohl, S. Cettour-Cave, K. Cornelis, H. Damerau, S. Gilardoni, M. Giovannozzi, C. Hernalsteens, A. Huschauer, V. Kain, D. Manglunki, G. Métral, B. Mikulec, B. Salvant, J. L. Sanchez Alvarez, R. Steerenberg, G. Sterbini, and Y. Wu, Operational performance of the CERN injector complex with transversely split beams, Phys. Rev. Accel. Beams **20**, 014001 (2017).

[7] A. Huschauer, A. Blas, J. Borburgh, S. Damjanovic, S. Gilardoni, M. Giovannozzi, M. Hourican, K. Kahle, G. Le Godec, O. Michels, G. Sterbini, and C. Hernalsteens, Transverse beam splitting made operational: Key features of the multi-turn extraction at the CERN Proton Synchrotron, Phys. Rev. Accel. Beams **20**, 061001 (2017).

[8] R. Cappi and M. Giovannozzi, Multiturn extraction: Performance analysis of old and new approaches, Nucl. Instrum. Methods Phys. Res., Sect. A **519**, 442 (2004).

[9] A. Bazzani, C. Frye, M. Giovannozzi, and C. Hernalsteens, Analysis of adiabatic trapping for quasi-integrable area-preserving maps, Phys. Rev. E **89**, 042915 (2014).

[10] A. Huschauer, H. Bartosik, S. Cettour Cave, M. Coly, D. Cotte, H. Damerau, G. P. Di Giovanni, S. Gilardoni, M. Giovannozzi, V. Kain, E. Koukovini-Platia, B. Mikulec, G. Sterbini, and F. Tecker, Approaching the high-intensity frontier using the multi-turn extraction at the cern proton synchrotron, in *Proceedings of the 61st ICFA ABDW HB2018, Daejeon, Korea*, edited by D. Jeon, D. Kim, and V. RW Schaa (JACoW Publishing, Geneva, Switzerland, 2018), pp. 231–236, 10.18429/JACoW-HB2018-WEA1WA02.

[11] A. Huschauer, H. Bartosik, S. Cettour Cave, M. Coly, D. Cotte, H. Damerau, G. P. Di Giovanni, S. Gilardoni, M. Giovannozzi, V. Kain, E. Koukovini-Platia, B. Mikulec, G. Sterbini, and F. Tecker, Advancing the CERN Proton Synchrotron multiturn extraction towards the high-intensity proton beams frontier, Phys. Rev. Accel. Beams **22**, 104002 (2019).

[12] A. Bazzani, C. Frye, M. Giovannozzi, and C. Hernalsteens, Analysis of adiabatic trapping for quasi-integrable area-preserving maps, Phys. Rev. E **89**, 042915 (2014).

[13] LHC Injectors Upgrade, Technical Design Report, Vol. **I**: Protons, Report No. CERN-ACC-2014-0337, edited by J. Coupard, H. Damerau, A. Funken, R. Garoby, S. Gilardoni, B. Goddard, K. Hanke, A. Lombardi, D. Manglunki, M.

Meddahi, B. Mikulec, G. Rumolo, E. Shaposhnikova, and M. Vretenar, CERN, Geneva, 2014.

[14] G. De Lellis, Search for hidden particles (SHiP): A new experiment proposal, Nucl. Part. Phys. Proc. **265**, 165 (2015).

[15] M. Anelli *et al.* (SHiP Collaboration), A facility to search for hidden particles (SHiP) at the CERN SPS, arXiv:1504.04956.

[16] S. Gilardoni, M. Giovannozzi, and C. Hernalsteens, First observations of intensity-dependent effects for transversely split beams during multiturn extraction studies at the CERN Proton Synchrotron, Phys. Rev. Accel. Beams **16**, 051001 (2013).

[17] S. Machida, C. Prior, S. Gilardoni, M. Giovannozzi, A. Huschauer, and S. Hirlander, Numerical investigation of space charge effects on the positions of beamlets for transversely split beams, Phys. Rev. Accel. Beams **20**, 121001 (2017).

[18] L. L. Foldy, A method for expanding the phase-stable regime in synchronous accelerators, Nuovo Cimento **19**, 1116 (1961).

[19] J. E. Griffin, C. Ankenbrandt, J. A. MacLachlan, and A. Moretti, Isolated bucket RF systems in the Fermilab antiproton facility, in *Proceedings of the 10th Particle Accelerator Conference (PAC83), Santa Fe, NM, 1983*, edited by L. S. Taylor (IEEE, New York, 1983), pp. 3502–3505.

[20] S. Y. Lee and K. Y. Ng, Particle dynamics in storage rings with barrier rf systems, Phys. Rev. E **55**, 5992 (1997).

[21] M. Fujieda, Y. Iwashita, A. Noda, Y. Mori, C. Ohmori, Y. Sato, M. Yoshii, M. Blaskiewicz, J. M. Brennan, T. Roser, K. S. Smith, R. Spitz, and A. Zaltsmann, Barrier bucket experiment at the AGS, Phys. Rev. ST Accel. Beams Beams, **2**, 122001 (1999).

[22] K. Y. Ng, Continuous multiple injections at the Fermilab Main Injector, Phys. Rev. Accel. Beams **5**, 061002 (2002).

[23] K. Takayama, Y. Arakida, T. Dixit, T. Iwashita, T. Kono, E. Nakamura, K. Otsuka, Y. Shimosaki, K. Torikai, and M. Wake, Experimental Demonstration of the Induction Synchrotron, Phys. Rev. Lett. **98**, 054801 (2007).

[24] S. Persichelli, M. Migliorati, M. Paoluzzi, and B. Salvant, in *Proceedings of the 5th International Particle Accelerator Conference, IPAC-2014, Dresden, Germany, 2014*, edited by C. Petit-Jean-Genaz, G. Arduini, P. Michel, and V. R. W. Schaa (JACoW, Geneva, 2014), paper TUPRI060, pp. 1708–1710.

[25] M. Paoluzzi and H. Damerau, Design of the PS longitudinal damper, Report No. CERN-ACC-NOTE-2013-0019, CERN, Geneva, 2013.

[26] M. Vadai, A. Alomainy, and H. Damerau, in *Proceedings of the 10th International Particle Accelerator Conference, IPAC-2019, Melbourne, Australia, 2019*, edited by F. Zimmermann *et al.* (JACoW, Geneva, 2019), paper MOPTS106, pp. 1128–1131.

[27] M. Vadai, A. Alomainy, H. Damerau, S. Gilardoni, M. Giovannozzi, and A. Huschauer, Barrier bucket and transversely split beams for loss-free multi-turn extraction in synchrotrons, Europhys. Lett. **128**, 14002 (2019).

[28] M. Vadai, A. Alomainy, H. Damerau, S. Gilardoni, M. Giovannozzi, and A. Huschauer, Beam manipulations with barrier buckets in the CERN PS, J. Phys. Conf. Ser. **1350**, 012088 (2019).

[29] G. Dome, in *CAS—CERN Accelerator School: Antiprotons for Colliding-Beam Facilities*, edited by P. J. Bryant and W. S. Newman (CERN, Geneva, 1983), pp. 215–260.

[30] CERN beam longitudinal dynamics code BLonD, http://blond.web.cern.ch.

[31] C. Lanczos, *Linear Differential Operators* (Martino Publishing, Mansfield Centre, 2012).

[32] L. Sermeus, M. J. Barnes, and T. Fowler, The kicker systems for the PS multi-turn extraction, in *Proceedings of the International Particle Accelerator Conference, Kyoto, Japan*, edited by Noda, Akira *et al.* (ICR, Kyoto, 2010), pp. 3311–3313.

[33] A. Hoffman and F. Pedersen, Bunches with local elliptic energy distributions, IEEE Trans. Nucl. Sci. **26**, 3526 (1979).

[34] T. Bohl, T. Linnecar, and E. Shaposhnikova, RF studies of the high intensity CNGS beam in the SPS, Report No. AB-Note-2005-034 MD, CERN, Geneva, 2005.

[35] E. Shaposhnikova, in Proceedings of the Laguna-LBNO General Meeting, CERN, Geneva, 2012 (unpublished).

[36] E. N. Shaposhnikova, E. Ciapala, and E. Montesinos, in *Proceedings of the 2nd International Particle Accelerator Conference, IPAC-2011, San Sebastián, Spain, 2019*, edited by C. Petit-Jean-Genaz *et al.* (JACoW, Geneva, 2011), paper MOPC058, pp. 214–2016.

[37] T. Bohl, T. Linnecar, E. Shaposhnikova, and J. Tueckmantel, in *Proceedings of the 6th European Particle Accelerator Conference, EPAC-1998, Stockholm, Sweden, 1998* (IOP, London, 1998), paper THP09A, pp. 978–980.

[38] E. Shaposhnikova, P. Baudrenghien, T. Bohl, T. Linnecar, and J. Tuckmantel, in *Proceedings of the 20th Particle Accelerator Conference, PAC-2003, Portland, OR, 2003* (IEEE, New York, 2003), paper RPPB015, pp. 3050–3052.

[39] E. Koukovini Platia, H. Bartosik, V. Forte, M. Giovannozzi, A. Huschauer, A. Lasheen, G. Rumolo, and E. Shaposhnikova, Beyond the LHC Injectors Upgrade Project, Report No. CERN-PBC-REPORT-2019-004, 2019.